

Gate-voltage control of alternating-current-driven skyrmion propagation in ferromagnetic nanotrack devices

Xin-Yi Cai(蔡心怡), Zhi-Hua Chen(陈志华), Hang-Xiao Yang(杨航霄), Xin-Yan He(何鑫岩), Zhen-Zhen Chen(陈珍珍), Ming-Min Zhu(朱明敏), Yang Qiu(邱阳), Guo-Liang Yu(郁国良), and Hao-Miao Zhou(周浩淼)

Citation: Chin. Phys. B, 2023, 32 (**6**): 067502. DOI: 10.1088/1674-1056/acb420
Journal homepage: http://cpb.iphy.ac.cn; http://iopscience.iop.org/cpb

What follows is a list of articles you may be interested in

Magnonic band-pass and band-stop filters with structurally modulated waveguides

Lai-He Feng(冯来和), Mang-Yuan Ma(马莽原), Zhi-Hua Liu(刘智华), Kai-Le Xie(解凯乐), and Fu-Sheng Ma(马付胜)

Chin. Phys. B, 2023, 32 (**6**): 067503. DOI: 10.1088/1674-1056/ac8afb

Magnetic triangular bubble lattices in bismuth-doped yttrium iron garnet

Tao Lin(蔺涛), Chengxiang Wang(王承祥), Zhiyong Qiu(邱志勇), Chao Chen(陈超), Tao Xing(邢弢), Lu Sun(孙璐), Jianhui Liang(梁建辉), Yizheng Wu(吴义政), Zhong Shi(时钟), and Na Lei(雷娜)

Chin. Phys. B, 2023, 32 (**2**): 027505. DOI: 10.1088/1674-1056/aca604

Skyrmion-based logic gates controlled by electric currents in synthetic antiferromagnet

Linlin Li(李林霖), Jia Luo(罗佳), Jing Xia(夏静), Yan Zhou(周艳), Xiaoxi Liu(刘小晰), and Guoping Zhao(赵国平)

Chin. Phys. B, 2023, 32 (**1**): 017506. DOI: 10.1088/1674-1056/ac9b01

Progress and challenges in magnetic skyrmionics

Haifeng Du(杜海峰) and Xiangrong Wang(王向荣)

Chin. Phys. B, 2022, 31 (**8**): 087507. DOI: 10.1088/1674-1056/ac754f

Current-driven dynamics of skyrmion bubbles in achiral uniaxial magnets

Yaodong Wu(吴耀东), Jialiang Jiang(蒋佳良), and Jin Tang(汤进)

Chin. Phys. B, 2022, 31 (**7**): 077504. DOI: 10.1088/1674-1056/ac6db1

Gate-voltage control of alternating-current-driven skyrmion propagation in ferromagnetic nanotrack devices

Xin-Yi Cai(蔡心怡)[1], Zhi-Hua Chen(陈志华)[2], Hang-Xiao Yang(杨航霄)[1], Xin-Yan He(何鑫岩)[1], Zhen-Zhen Chen(陈珍珍)[1], Ming-Min Zhu(朱明敏)[1], Yang Qiu(邱阳)[1], Guo-Liang Yu(郁国良)[1,†], and Hao-Miao Zhou(周浩淼)[1,‡]

[1] *Key Laboratory of Electromagnetic Wave Information Technology and Metrology of Zhejiang Province, College of Information Engineering, China Jiliang University, Hangzhou* 310018, *China*
[2] *Zhejiang Chunhui Magnetoelectric Technology Co., Ltd, Shaoxing* 312300, *China*

(Received 26 November 2022; revised manuscript received 10 January 2023; accepted manuscript online 18 January 2023)

Magnetic skyrmions, with topologically protected particle-like magnetization configurations, are promising information carriers for future spintronics devices with ultralow energy consumption. Generally, during motion, skyrmions suffer from the skyrmion Hall effect (SkHE) wherein the skyrmions deflect away from the intended path of the driving force. Numerous methods have been proposed to avoid this detrimental effect. In this study, we propose controllable alternating current (AC)-driven skyrmion propagation in a ferromagnetic nanowire based on combination of gate-voltage-controlled magnetic anisotropy (VCMA) and SkHE. Micromagnetic simulations show that a skyrmion oscillatory closed-loop-like *in situ* motion driven by AC can be transformed into directional ratchet-like propagation along the nanotrack by creating a VCMA-gate barrier. Additionally, we show that the skyrmion propagation conditions depend on the gate barrier potential and driving AC parameters, and they can be used for the optimal design of nanotrack devices. Moreover, this mechanism could be used to control skyrmion macroscopic propagation directions by dynamically alternating the voltage of another series of gates. We further show the dynamic control of the long-distance propagation of skyrmions along with the pinning state. The study results provide a promising route for designing future skyrmion-based spintronics logical and memory devices.

Keywords: skyrmion, voltage-controlled magnetic anisotropy, Hall effect, net propagation

PACS: 75.40.Mg, 75.60.Ch, 75.78.Cd **DOI:** 10.1088/1674-1056/acb420

1. Introduction

Magnetic skyrmions are nanoscale magnetization structures with topologically protected stability, and they have been discovered in non-centrosymmetric magnetic bulk crystals and ultrathin ferromagnetic films in the presence of bulk and interfacial Dzyaloshinskii–Moriya interaction (iDMI).[1] Owing to their unique topological stability, ultra-low driving current, and extremely small size, magnetic skyrmions are promising information carriers for the future spintronic devices, such as racetrack memory for bit data storage,[2,3] logic system for large-scale Boolean computation,[4,5] spin-transfer torque oscillator for microwave signal generator,[6] and artificial neural devices for neuromorphic computing.[7]

The fundamental manipulations of skyrmions, including the nucleation/annihilation, propagation, and detection of skyrmions, have been intensively studied theoretically and experimentally.[8–11] Nevertheless, the controllable skyrmion propagation characteristics in the practical racetrack memory, e.g., pining/depinning and switching motion direction as required, are indispensable. Several different methods have been proposed to drive skyrmions. They can be driven by providing external stimuli, such as microwave magnetic field,[12] spin wave,[13] voltage-controlled magnetic anisotropy (VCMA) gradient,[14] strain gradient,[15] optical vortices beam,[16] thermal gradients,[17] and spin polarized current.[18] Additionally, skyrmions can be pinned using the VCMA barrier, strain-induced magnetoelastic barrier, and geometric notches.[19–21] Recently, Wang *et al.* theoretically showed that skyrmions can be pinned by disk-shaped defects.[22] On the other hand, skyrmions tend to experience a transverse deflection from the intended path of the driving force, which is known as the skyrmion Hall effect (SkHE), owing to the transverse Magnus force associated with nonzero topological skyrmion charge.[23,24] Subsequently, several methods have been proposed to overcome or eliminate SkHE. For example, SkHE (stemming from nonzero topological skyrmion charges) and magnetic spin textures (i.e., skyrmioniums) with zero topological charge can strictly propagate along the nanotrack without SkHE.[25] However, the large deformations induced by the separation of their core and shell during propagation will make them hard to detect. Furthermore, the application of another force to compensate for the Magnus force has been realized by locally changing the perpendicular magnetic anisotropy (PMA) and DMI coefficients,[26–29] as well as by engineering defects such as lines,[30] kerbs,[31] edge spin textures,[32] and bilayer magnetic systems.[33] However, recent studies

†Corresponding author. E-mail: glyu@cjlu.edu.cn
‡Corresponding author. E-mail: zhouhm@cjlu.edu.cn

© 2023 Chinese Physical Society and IOP Publishing Ltd

have shown that the SkHE can be utilized, instead of being suppressed, e.g., skyrmion-based programmable logic gates, wherein logic functions are dependent on the SkHE and specific PMA changes.[4,5] Different from DC driven approaches, Göbel *et al.* numerically studied alternating current (AC)-driven skyrmion propagation based on the "hollowing" ratchet mechanism.[34] Although the directional transportation of skyrmion has been realized, dynamically controlling the propagation direction of skyrmions as required is not effective.

In this study, the macroscopic propagation of AC-driven skyrmions is dynamically controlled by applying VCMA gates on the ferromagnetic material. Extensive experiments were conducted to characterize the VCMA physical parameters and verify the controller performance.[35–37] The application of VCMA gates induces asymmetric PMA of the nanowire along the width direction. This anisotropy can induce an energy barrier, drive skyrmions to not cross the gates, and finally, transform the skyrmion gyration into directional transportation along the length direction of the nanotrack. The propagation states are dependent on the geometric parameters of the VCMA gates as well as the frequency and amplitude of the applied AC. Furthermore, the dynamic control of VCMA allows the pinning of skyrmions at specific positions without applying voltage on the gates and allows the switching of the propagation direction by dynamically alternating the voltage of another series of gates. This dynamic manipulation presents the possibility of using VCMA gates to control the motion of AC-driven skyrmions, providing an attractive alternative for using SkHE rather than suppressing it.

2. Model and details

Magnetization dynamics in a ferromagnetic material are governed by the Landau–Lifshitz–Gilbert equation with spin Hall effect (SHE) torques

$$\frac{\partial \boldsymbol{m}}{\partial t} = -\gamma \boldsymbol{m} \times \boldsymbol{H}_{\text{eff}} + \alpha \boldsymbol{m} \times \frac{\partial \boldsymbol{m}}{\partial t} + \boldsymbol{\tau}_{\text{SHE}}, \tag{1}$$

where $\boldsymbol{m} = \boldsymbol{M}/M_{\text{s}}$ represents the spatial distribution of the reduced local magnetization vector, M_{s} denotes the saturation magnetization, μ_0 is the vacuum permeability, γ is the gyromagnetic ratio, and α is the Gilbert damping parameter. $\boldsymbol{H}_{\text{eff}} = -1/\mu_0 M_{\text{s}} \cdot \partial E/\partial \boldsymbol{m}$ is the effective magnetic field. In our proposed system, the total energy density comprises the PMA, ferromagnetic exchange, iDMI, and demagnetization energy terms. Thus, the effective magnetic field reads

$$\begin{aligned} \boldsymbol{H}_{\text{eff}} = & \frac{2K_{\text{u}}}{\mu_0 M_{\text{S}}} m_z \boldsymbol{e}_z + \frac{2A_{\text{ex}}}{\mu_0 M_{\text{S}}} \nabla^2 \boldsymbol{m} + \boldsymbol{H}_{\text{d}}(\boldsymbol{m}) \\ & + \frac{2D}{\mu_0 M_{\text{S}}} \left[(\nabla \cdot \boldsymbol{m}) \boldsymbol{e}_z - \nabla m_z \right], \end{aligned} \tag{2}$$

where A_{ex}, K_{u}, and D represent the exchange, PMA, and iDMI energy constants, respectively; $\boldsymbol{H}_{\text{d}}(\boldsymbol{m})$ is the demagnetization field; $\boldsymbol{e}_z$ is the out-of-plane unit surface normal vector; and m_z is the out-of-plane component of $\boldsymbol{m}$. In our simulated system, the SHE torque can be written as[18]

$$\boldsymbol{\tau}_{\text{SHE}} = -\gamma_0 \boldsymbol{m} \times \left(\boldsymbol{m} \times \frac{\hbar \theta_{\text{SHE}} J_{\text{HM}}}{2\mu_0 e M_{\text{s}} t_{\text{FM}}} \boldsymbol{e}_y \right), \tag{3}$$

where e is the electron charge, $\hbar$ is the reduced plank constant, θ_{SHE} is the spin Hall angel, t_{FM} is the thickness of the ferromagnetic nanotrack, and J_{HM} is the current density.

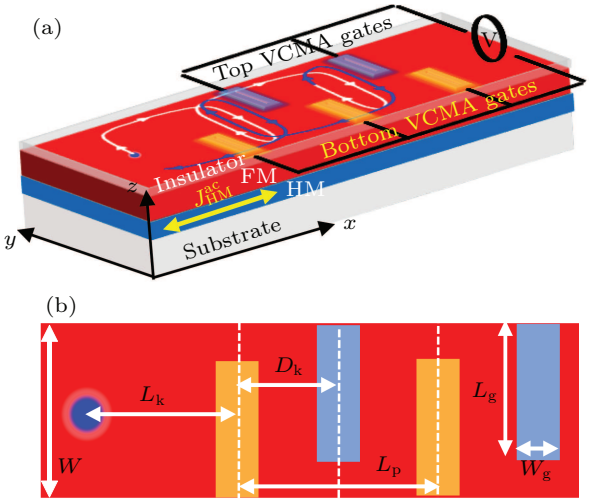


Fig. 1. Design of the proposed voltage-controlled skyrmion-based nanotrack device. (a) Schematic view of the voltage-controlled AC-driven skyrmion net propagation in the nanotrack. Two groups of VCMA gates are cross placed at the top and bottom edges of the nanotrack. The white and blue arrow lines attached to the skyrmion illustrate the trajectory when the bottom (light yellow) and top (light blue) VCMA gates are working. The AC current is applied in the HM layer. (b) Closeup view (*xy*-plane) of the proposed VCMA-gates-controlled nanotrack.

Figure 1 displays the structure of the proposed device, which comprises 2-nm-thick Co/Pt heavy ferromagnetic/heavy metal layers placed on the substrate and is covered with an oxide layer (i.e., MgO). The width and length of the nanotrack are denoted by W and L, respectively. Two series of the voltage-controlled gates of $W_{\text{g}} \times L_{\text{g}} = 30$ nm $\times$ 80 nm are periodically placed on the top surface of the oxide layer with distance L_{P} and D_{k}; see Fig. 1(b) for the detailed configuration. When no voltage is applied to the gates, the skyrmions periodically move in a closed trajectory driven by AC due to SkHE, and such motion does not exhibit net propagation. When voltage is applied to the gates, an electric field traverses across the structure and induces charge accumulation at the interface between the nanotrack and oxide layers. The surface magnetic anisotropy changes with the applied electric field, and finally, an energy barrier or well forms locally. This VCMA modulates the local anisotropy field under the gates and induces a periodic (length direction), spatially non-symmetric (width direction) distribution of the anisotropy field, thus breaking the AC-driven skyrmion closed trajectory and resulting in a net propagation along the length direction (the white and blue arrow lines in Fig. 1(a)).

Micromagnetic simulations were performed using GPU accelerate open source software Mumax^3,[38] and the mesh

cell dimension was 2 nm × 2 nm × 2 nm. The material parameters of the Co/Pt multilayer in our simulations were as follows: Gilbert damping $\alpha = 0.3$, exchange constant $A_{ex} = 1.5 \times 10^{-11}$ J/m, iDMI constant $D = 3 \times 10^{-3}$ J/m^2, saturation magnetization $M_s = 5.8 \times 10^5$ A/m, uniaxial anisotropy constant $K_u = 8 \times 10^5$ J/m^2, and spin hall angle $\theta_{SHE} = 0.3$. Based on previous studies, the PMA values within the voltage-gated region can be assumed to linearly vary with the electric field $K_{uv} = K_u + \Delta K_{uv} E_g$.[39] In the simulation, when voltage is applied on the gates, the PMA values of the gate region are directly set, i.e., $K_{uv} = \xi K_u$ ($\xi > 1$ means forming an energy barrier within the gate region, while $\xi < 1$ denotes the energy well).

3. Results and discussion

First, the gyration modes of a skyrmion driven by an AC without applied voltage on the gates are examined. A magnetic skyrmion is created and relaxed using a current-induced skyrmion injector, which can be fabricated by placing a magnetic tunnel junction on a nanotrack. Then, an oscillating current, $J_{HM} = e_x J_{HM} \sin(2\pi f_{ac}^{J_{HM}} t)$, with various frequencies $f_{ac}^{J_{HM}}$ and amplitudes J_{HM} is applied. To understand the skyrmion trajectories, two typical current amplitudes are employed, and the corresponding snapshot images are extracted from the simulation and plotted in Fig. 2(a). Here, $f_{ac}^{J_{HM}} = 50$ MHz, and the amplitudes for the gyration and annihilation cases are set as 3×10^{11} A/m^2 and 6×10^{11} A/m^2, respectively. Clearly, the skyrmion starts to move from the initial position in a diagonal direction after the current is applied due to the SkHE. In the gyration case, the skyrmion finally exhibits a clockwise rotation with the same frequency as the oscillation current (the white and blue lines correspond to the positive and negative current half period, respectively). On the other hand, in the annihilation case, the skyrmion approaches the edge of the track and starts to get annihilated within the first positive current period.

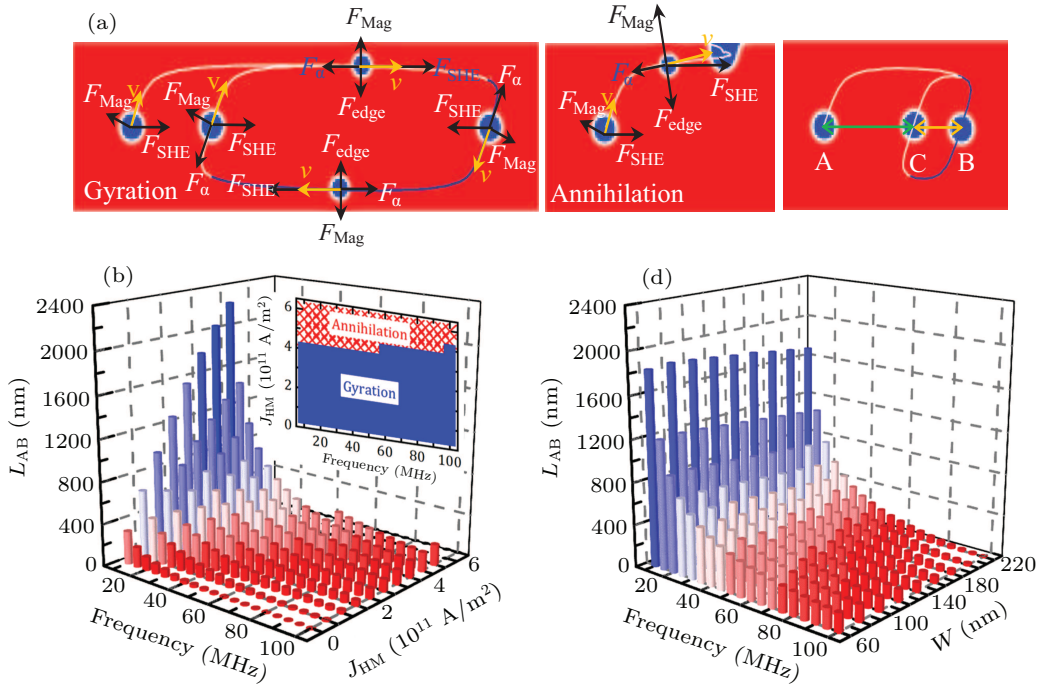


Fig. 2. (a) The trajectory of a skyrmion driven by an AC current under gyration and annihilation conditions. The white and blue solid lines represent the skyrmion trace of the positive and negative half periods, respectively. The schematic diagrams of the forces exerting on the skyrmion at different positions are given. The last panel displays the distance definition at $y = 0$. (b) L_{AB} versus frequency and amplitude. The inset shows the phase diagram of the skyrmion moving cases under different current amplitudes and frequencies. (c) L_{AB} versus frequency and nanotrack width.

To clearly illustrate the different results, the analytical model of the rigid skyrmion motion called Thiele's equation is used, which can be written as

$$\boldsymbol{G} \times \boldsymbol{v} - \overleftrightarrow{\boldsymbol{D}} \cdot \boldsymbol{v} + \boldsymbol{F}_{SHE} + \boldsymbol{F}_{edge} + \boldsymbol{F}_{VCMA} = 0, \tag{4}$$

where $\boldsymbol{v} = \mathrm{d}\boldsymbol{X}/\mathrm{d}t$ is the velocity of the skyrmion which can be decomposed by the skyrmion position $\boldsymbol{X} = (X, Y)$ into the length ($\boldsymbol{e}_x$) and width ($\boldsymbol{e}_y$) directions. The first term of Eq. (4) represents the Magnus force $\boldsymbol{F}_{mag}$, and $\boldsymbol{G} = 4\pi Q \boldsymbol{e}_z$ is the so-called gyrocoupling vector; $Q = \frac{1}{4\pi} \int \mathrm{d}r^2 \boldsymbol{m} \left(\frac{\partial \boldsymbol{m}}{\partial x} \times \frac{\partial \boldsymbol{m}}{\partial y} \right)$ is the topological number. The second term represents the damping force $\boldsymbol{F}_\alpha$, and $\overleftrightarrow{\boldsymbol{D}}$ is the damping tensor with the elements $D_{xx} = D_{yy} = \alpha \int \mathrm{d}r^2 \frac{\partial \boldsymbol{m}}{\partial x} \frac{\partial \boldsymbol{m}}{\partial y}$, $D_{xy} = D_{yx} = 0$. The third term represents the current-induced driving force with the form $\boldsymbol{F}_{SHE} = \sigma k J_{HM} \boldsymbol{e}_z \times \boldsymbol{e}_y$; its value is proportional to that of the current density, $\sigma = -\pi\hbar\theta_{SHE}/2e$. Here, k is the characteristic length of the skyrmion. Note that an applied current $\boldsymbol{J}_{HM} \parallel \pm \boldsymbol{e}_x$ leads to an injection of spin $\parallel \pm \boldsymbol{e}_y$ from the perpendicular di-

rection. Thus, the $\boldsymbol{F}_{\rm SHE}$ direction is dependent on the applied current direction. $\boldsymbol{F}_{\rm edge}$ represents the repulsive force when the skyrmion approaches the nanotrack edges. In our proposed model, $\boldsymbol{F}_{\rm edge}$ only has the $\boldsymbol{e}_y$ component due to the finite width, and they confine the skyrmion to always stay inside the nanotrack. This implies that without the driving force, the equilibrium position of the skyrmion will be in the center of nanotrack due to the edge effect. $\boldsymbol{F}_{\rm VCMA}$ represents the force induced by the VCMA when the skyrmion approaches the gates. Notably, $\boldsymbol{F}_{\rm VCMA}$ is dependent on the skyrmion relative position with the gate's region and its potential type, i.e., energy barrier or energy well. Note that energy well is not considered here. The schematic of the force exerting on the skyrmion at different positions is given in Fig. 2(a) with a black arrow, while the yellow arrow represents the velocity direction of the skyrmion. Based on the analytical expression in Eq. (4), the damping force is always antiparallel to the velocity direction, the Magnus force is perpendicular to the velocity direction, and the driving force is dependent on the current direction. Thus, under the oscillation current without an applied voltage, the net driving force compels the skyrmion to oscillate in closed gyration. First, the skyrmion accelerates along $+x$ and $+y$ toward the upper edge due to the increase of the current density during the first quarter period (0–$T/4$; $T = 1/f$). During the next quarter period ($T/4$–$T/2$), the skyrmion decelerates and glides along the $+x$ direction due to the decrease of the current density. The trajectories of this half period (0–$T/2$) is shown with a white trace line in Fig. 2(a). Moreover, the Magnus force decreases with the velocity and the skyrmion slightly moves toward the $-y$ direction due to the edge force. Once the half period $T/2$ with positive current ends, the current becomes negative ($T/2$–T). Then, the skyrmion accelerates and moves along $-x$ and $-y$ to the lower edge, and thereafter, it decelerates along $-x$ and slightly along $+y$, as indicated by the blue trace line in Fig. 2(a). The moving direction is not immediately switched due to the damping effect. After a full period (0–T), the current becomes positive again. The skyrmion starts moving toward the upper edge of the nanotrack and continually oscillates in a closed gyration. Specially, the compensation effect between the Magnus force and the edge force is limited by the physical edge of the nanotrack. In the annihilation case, the skyrmion is clearly destroyed at the nanotrack edge when a large current is applied. To further use the VCMA effect on the gates to effectively control the skyrmion motion, the skyrmion moving cases are summarized and a distance between the cross point of the center axis with the trajectories is extracted at different current densities and frequencies, as shown in Fig. 2(b). Here, the nanotrack width is fixed as $W = 120$ nm. As shown in the inset of Fig. 2(b), the threshold current density slightly increases with the frequency. Nevertheless, the propagation distance $L_{\rm AB}$ between AB sharply decreases with increasing frequency. Figure 2(c) depicts $L_{\rm AB}$ as a function of the frequency and nanotrack width. Here, the current density is fixed as $J_{\rm HM} = 3 \times 10^{11}$ A/m^2. The distance exhibits same trends for different nanotrack widths. All these results indicate that only *in situ* closed motion can be realized when the oscillation current is applied and the distance $L_{\rm AB}$ can be controlled by the oscillation current.

As mentioned above, the VCMA barrier is introduced to break the symmetry and to achieve a net propagation of skyrmion. We now study the behavior of skyrmion gyration when VCMA barrier is formed by the voltage gates proposed in Fig. 1. Here, the frequency and amplitude are set as 80 MHz and 3×10^{11} A/m^2, respectively. $L_{\rm AB}$ and $L_{\rm AC}$ are about 166 nm and 74.5 nm, respectively, based on the simulation results when no voltage is applied to the gates, as shown in Fig. 2. Importantly, the skyrmion first reaches the voltage gate region and traverses through it or is repulsed, which is dependent on the gate position and barrier potential. Furthermore, the instantaneous current density when the skyrmion approaches the barrier is dependent on the gate positions due to the sinusoidal time-dependent oscillation. Similar to the physical edge, when the skyrmion approaches the gate, it experiences a force $\boldsymbol{F}_{\rm VCMA}$ component along the $\pm x$ direction, which is dependent on the skyrmion position. Thus, given a specific driving oscillation current, whether a skyrmion can be blocked by the VCMA-gated region is dependent on the competition between the instantaneous current force and the VCMA force. $L_{\rm k}$ represents the distance between the skyrmion initial position and the first VCMA gate. Figure 3(a) displays the phase diagram of skyrmion behavior after the application of $3T/2$ of the oscillation current when the VCMA barrier forms at different distances $L_{\rm k}$ and coefficients ξ. Three cases are considered: (I) Obviously, when the voltage is turned off, i.e., $\xi = 1$, or the voltage is turned on ($\xi > 1$) and the $L_{\rm k}$ is smaller than 70 nm or larger than 180 nm, the skyrmion always gyrates in a closed loop due to the lack of the VCMA energy barrier effect. (Ⅱ) When the driving force overcomes the energy barrier, the skyrmion passes the VCMA-gate region and moves toward the $-x$ direction. (Ⅲ) When the driving force cannot overcome the energy barrier, the skyrmion is block by the VCMA-gate region and moves toward to the $+x$ direction. Figure 3(b) displays the typical trajectory and snapshots of the skyrmion motion corresponding to Fig. 3(a). It shows that the skyrmion oscillation can be transformed to the net propagation due to the VCMA-barrier-induced anisotropy to break the balance between the backward and forward propagations, see the cases Ⅲa, Ⅲb, and Ⅲc. In the cases Ⅲa and Ⅲb, when the skyrmion under the negative half period, the skyrmion will move along $-x$ direction, as shown by the blue trajectory line in Fig. 3(b). When the skyrmion approaches to the VCMA gate region, a repulsive VCMA force induced by the higher magnetic anisotropy will exert on the skyrmion and force it to

move away from the gate region. At the same time, the negative half-period current density gradually decreases, and the next positive half period begins. Thus, the skyrmion will start to propagate in the $+x$ direction. As shownin Fig. 3(b) for the cases Ⅱb and Ⅱc, although a net propagation appears after $3T/2$ current driving, placing another VCMA-gate to realize an efficient net $+x$ direction propagation during another period current is not convenient. Note that the skyrmion shrinks when it approaches the voltage-gate region, which is consistent with the previous studies.[40]

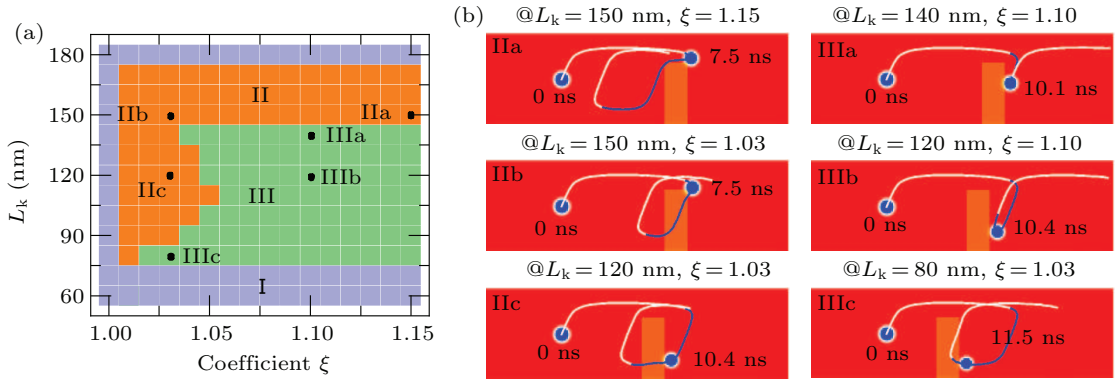


Fig. 3. (a) Phase diagram of the skyrmion moving states with various VCMA-gates distances L_k and coefficients ξ. (b) The typical trajectory and magnetization snapshots of the skyrmion motion corresponding to the cases marked in (a).

To investigate the current density induced skyrmion moving states with various VCMA-gates coefficient ξ, we have also carried out a phase diagram with fixed VCMA-gates distance L_k at frequency $f_{ac}^{HM} = 80$ MHz. As illustrated in Fig. 4(a), the same cases as described in Fig. 3(a) are observed. The trajectories of Ⅱd and Ⅱe in Fig. 4(b) show a same manner as Ⅱb and Ⅱa in Fig. 3(b), respectively. In addition, the case Ⅳ indicates that the skyrmion annihilates during the half positive period which is independent of the coefficient ξ. This annihilation current density coincides with the simulation results shown in the inset of Fig. 2(b). From interface of cases Ⅱ and Ⅲ in the phase diagram, one can see that the maximum current density driven skyrmion blocked by the VCMA gates increases as the coefficient ξ increases. In other words, at the same current density, the VCMA force is larger for a skyrmion with larger coefficient ξ.

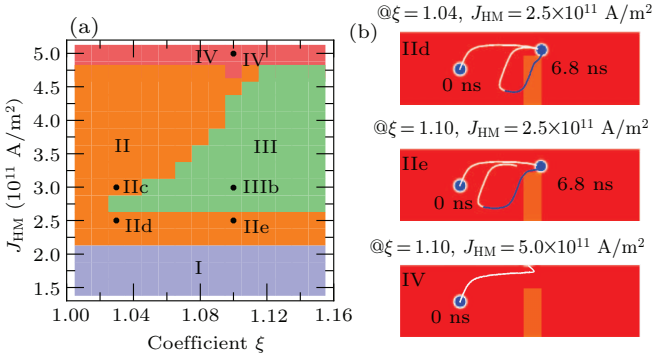


Fig. 4. (a) Phase diagram of the skyrmion moving states with various VCMA-gates coefficients ξ and current densities. (b) The typical trajectory and magnetization snapshots of the skyrmion motion corresponding to (a).

In such skyrmion-based devices, long-distance controllable propagation is required. Next, the influence of the oscillation current frequency and amplitude is investigated, and controllable propagation modes in periodically VCMA gate region structures are presented. Here, the periodic distance L_p is fixed at 150 nm, and $K_{uv} = 1.10K_u$. Initially, the current density is $J_{HM} = 3 \times 10^{11}$ A/m^2 and frequency is $f_{ac}^{HM} = 80$ MHz; the propagation trajectory is shown in the top panel of Fig. 5(a). A well-period one-step motion can be realized. Generally, the transient process from the initial position to the periodic motion is affected by the oscillation current and L_k. However, for typical parameters, this effect can be canceled when the step distance L_p is smaller than the distance L_{AB}. Thus, the trajectory in Fig. 5 is simplified by excluding the started transient process. In the second and third panels of Fig. 5(a), two- and three-step propagation modes are presented. As given in Fig. 2, the distance L_{AB} increases as the frequency decreases. Thus, the propagation distance increases per period. The velocity, i.e., the propagation distances normalized by the period ($T = 1/f$) corresponding to the three modes are 12 m/s, 14.98 m/s, and 13.56 m/s, respectively. Therefore, this diagram can be used to design controllable multi-step mode propagation schemes by choosing a specific AC. The inset in Fig. 5(b) displays the design of the applied current and time sequence evolution of these modes. Totally, six switchings between the above three step modes are simulated, and the x position of the skyrmion over time is shown in Fig. 5(b).

So far, the current parameters have been adjusted to control the skyrmion propagation so that multi-step motion is realized. In the following, to investigate the VCMA-controlled propagation directions, another periodic VCMA gate centered between the previous ones is added ($D_k = 75$ nm) and aligned on the top edge of the nanotrack, as shown by the light blue gates in Fig. 1. Figure 6(a) shows the $+x$ net propagation when the bottom VCMA gates work and $-x$ net propagation when the top VCMA gates work. When the VCMA gates switch to the top series, the skyrmion continually moves under the

oscillation current until it approaches the top VCMA gate region, and then, it moves along the $-x$ and $-y$ directions towards the bottom edge, thereafter it glides along the $-x$ direction. The period exhibits $-x$ net propagation with the same propulsion mechanism. Based on the simulations, continuously controlled skyrmion motion through VCMA is shown in Fig. 6(b). By applying a voltage on the bottom VCMA gates, regions with higher magnetic anisotropy cause the skyrmion to move along the $+x$ direction. Then, the voltage on the bottom VCMA gates is turned off. This removes the modulation of the anisotropy, and the skyrmion exhibits a loop motion (which can be regarded as a pinning case) without net propagation until the voltage is switched on. When the voltage on the bottom VCMA gates is turned off and that on the top VCMA gates is turned on, the anisotropy modulation will force the skyrmion to move along the $-x$ direction, as shown by the black curve in Fig. 6(b).

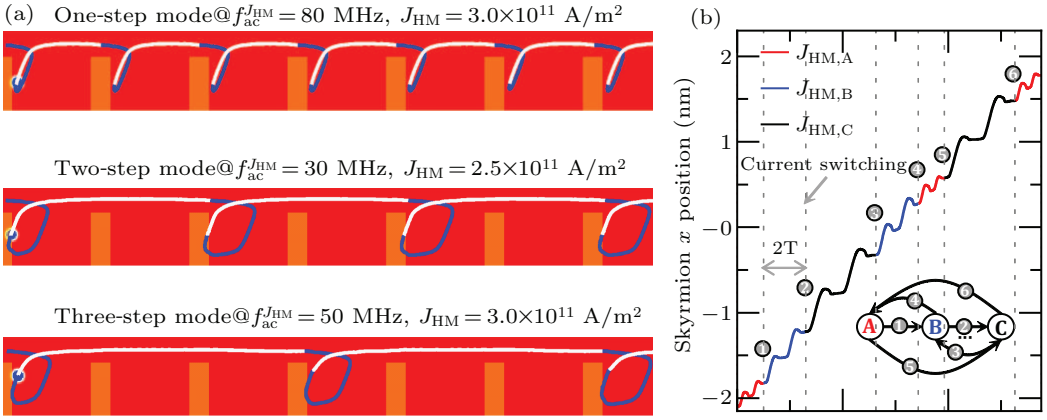


Fig. 5. (a) The propagation trajectory and magnetization snapshot of skyrmions with current $J_{HM,A}$ ($f_{ac}^{HM} = 80$ MHz, $J_{HM} = 3.0 \times 10^{11}$ A/m^2) in one-step mode (first panel), current $J_{HM,B}$ ($f_{ac}^{HM} = 50$ MHz, $J_{HM} = 3.0 \times 10^{11}$ A/m^2) in two-step mode (second panel), and current $J_{HM,C}$ ($f_{ac}^{HM} = 30$ MHz, $J_{HM} = 2.5 \times 10^{11}$ A/m^2) in three-step mode (third panel). (b) The skyrmion position of the series of step mode dynamic switching. The inset shows the switching process of the step modes.

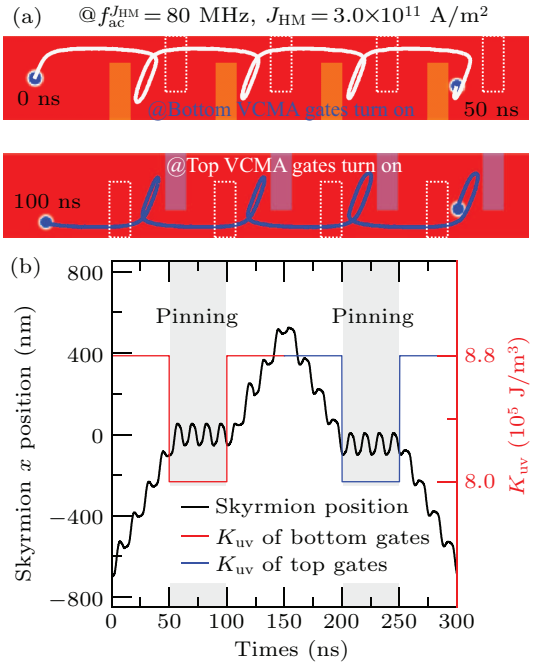


Fig. 6. (a) The net-propagation trajectory and magnetization snapshot of the skyrmion when the bottom VCMA gates working (top panel) and the top VCMA gates working (bottom panel). (b) The position of the skyrmion under series VCMA gate working conditions.

4. Conclusion

We have reported voltage-controlled AC-induced skyrmion net propagation assisted by a periodical VCMA gates region within a nanotrack. The VCMA gates region forms a local energy barrier and induces the VCMA force along either the $+x$ or $-x$ direction to transform the closed loop motion into directed motion along the nanotrack. Additionally, the propagation mode can be manipulated by varying the amplitude and frequency of the oscillation current. Furthermore, this mechanism can control the skyrmion macroscopic propagation direction by dynamically alternating the voltage of another series of gates. The present results illustrate the physical mechanism for the voltage tunability of skyrmion propagation under the AC excitation, which is significant for designing AC-driven skyrmion-based devices.

Acknowledgements

Project supported by the National Natural Science Foundation of China (Grant Nos. 51902300, 11972333, and 11902316), the Natural Science Foundation of Zhejiang Province, China (Grant Nos. LY21F010011, LZ19A020001, and LZ23A020002), and the Fundamental Research Funds for the Provincial Universities of Zhejiang (Grant Nos. 2021YW02 and 2022YW88). G. L. Yu also acknowledges a start-up fund from the China Jiliang University. The simulations were aided by the Key Laboratory of Electromagnetic Wave Information Technology and Metrology of Zhejiang Province.

References

[1] Fert A, Cros V and Sampaio J 2013 *Nat. Nanotechnol.* **8** 152

[2] Luo S and You L 2021 *APL Mater.* **9** 050901

[3] Parkin S S, Hayashi M and Thomas L 2008 *Science* **320** 190

[4] Chauwin M, Hu X, Garcia-Sanchez F, Betrabet N, Paler A, Moutafis C and Friedman J S 2019 *Phys. Rev. Appl.* **12** 064053

[5] Luo S, Song M, Li X, Zhang Y, Hong J, Yang X, Zou X, Xu N and You L 2018 *Nano Lett.* **18** 1180

[6] Yu G, Xu X, Qiu Y, Yang H, Zhu M and Zhou H 2021 *Appl. Phys. Lett.* **118** 142403

[7] Zhu M M, Cui S T, Xu X F, Shi S B, Nian D Q, Luo J, Qiu Y, Yang H, Yu G L and Zhou H M 2022 *Chin. Phys. B* **31** 018503

[8] Gobel B, Schaffer A F, Berakdar J, Mertig I and Parkin S S P 2019 *Sci. Rep.* **9** 12119

[9] Wang Y, Wang L, Xia J, Lai Z, Tian G, Zhang X, Hou Z, Gao X, Mi W, Feng C, Zeng M, Zhou G, Yu G, Wu G, Zhou Y, Wang W, Zhang X X and Liu J 2020 *Nat. Commun.* **11** 3577

[10] Ba Y, Zhuang S, Zhang Y, Wang Y, Gao Y, Zhou H, Chen M, Sun W, Liu Q, Chai G, Ma J, Zhang Y, Tian H, Du H, Jiang W, Nan C, Hu J M and Zhao Y 2021 *Nat. Commun.* **12** 322

[11] Qiu S, Liu J H, Chen Y B, Zhao Y P, Wei B and Fang L 2022 *Chin. Phys. B* **31** 117701

[12] Wang W, Beg M, Zhang B, Kuch W and Fangohr H 2015 *Phys. Rev. B* **92** 020403

[13] Zhang X, Ezawa M, Xiao D, Zhao G P, Liu Y and Zhou Y 2015 *Nanotechnology* **26** 225701

[14] Xia H, Song C, Jin C, Wang J, Wang J and Liu Q 2018 *J. Magn. Magn. Mater.* **458** 57

[15] Yanes R, Garcia-Sanchez F, Luis R F, Martinez E, Raposo V, Torres L and Lopez-Diaz L 2019 *Appl. Phys. Lett.* **115** 132401

[16] Yang W, Yang H, Cao Y and Yan P 2018 *Opt. Express* **26** 8778

[17] Raimondo E, Saugar E, Barker J, Rodrigues D, Giordano A, Carpentieri M, Jiang W, Chubykalo-Fesenko O, Tomasello R and Finocchio G 2022 *Phys. Rev. Appl.* **18** 024062

[18] Song C, Jin C, Wang J, Xia H, Wang J and Liu Q 2017 *Appl. Phys. Lett.* **111** 192413

[19] Kang W, Huang Y, Zheng C, Lv W, Lei N, Zhang Y, Zhang X, Zhou Y and Zhao W 2016 *Sci. Rep.* **6** 23164

[20] Li Z, Zhang Y, Huang Y, Wang C, Zhang X, Liu Y, Zhou Y, Kang W, Koli S C and Lei N 2018 *J. Magn. Magn. Mater.* **455** 19

[21] Ding J, Yang X and Zhu T 2015 *J. Phys. D: Appl. Phys.* **48** 115004

[22] Gong X, Jing K Y, Lu J and Wang X R 2022 *Phys. Rev. B* **105** 094437

[23] Jiang W, Zhang X, Yu G, Zhang W, Wang X, Benjamin Jungfleisch M, Pearson John E, Cheng X, Heinonen O, Wang K L, Zhou Y, Hoffmann A and te Velthuis Suzanne G E 2016 *Nat. Phys.* **13** 162

[24] Litzius K, Lemesh I, Krüger B, Bassirian P, Caretta L, Richter K, Büttner F, Sato K, Tretiakov O A, Förster J, Reeve R M, Weigand M, Bykova I, Stoll H, Schütz G, Beach G S D and Kläui M 2016 *Nat. Phys.* **13** 170

[25] Kolesnikov A G, Stebliy M E, Samardak A S and Ognev A V 2018 *Sci. Rep.* **8** 16966

[26] Zhang Y, Luo S, Yan B, Ou-Yang J, Yang X, Chen S, Zhu B and You L 2017 *Nanoscale* **9** 10212

[27] Lai P, Zhao G P, Tang H, Ran N, Wu S Q, Xia J, Zhang X and Zhou Y 2017 *Sci. Rep.* **7** 45330

[28] Liu G B, Li D, P F d C, Wang J, Liu W and Zhang Z D 2016 *Chin. Phys. B* **25** 067203

[29] Bhatti S and Piramanayagam S N 2019 *Phys. Status Solidi RRL* **13** 1900090

[30] Castell-Queralt J, González-Gómez L, Del-Valle N, Sanchez A and Navau C 2019 *Nanoscale* **11** 12589

[31] Purnama I, Gan W L, Wong D W and Lew W S 2015 *Sci. Rep.* **5** 10620

[32] Xing X, Åkerman J and Zhou Y 2020 *Phys. Rev. B* **101** 214432

[33] Zhang X, Zhou Y and Ezawa M 2016 *Nat. Commun.* **7** 10293

[34] Gobel B and Mertig I 2021 *Sci. Rep.* **11** 3020

[35] Tan F N, Lim G J, Jin T L, Liu H X, Poh F and Lew W S 2019 *J. Magn. Magn. Mater.* **490** 165448

[36] Bhattacharya D, Razavi S A, Wu H, Dai B, Wang K L and Atulasimha J 2020 *Nat. Electron.* **3** 539

[37] Yang S, Son J W, Ju T S, Tran D M, Han H S, Park S, Park B H, Moon K W and Hwang C 2022 *Adv. Mater.* **35** e2208881

[38] Vansteenkiste A, Leliaert J, Dvornik M, Helsen M, Garcia-Sanchez F and Van Waeyenberge B 2014 *AIP Adv.* **4** 107133

[39] Wang Q, Chumak A V, Jin L, Zhang H, Hillebrands B and Zhong Z 2017 *Phys. Rev. B* **95** 134433

[40] Zhang X, Zhou Y, Ezawa M, Zhao G P and Zhao W 2015 *Sci. Rep.* **5** 11369